Ultra-Stretchable Spiral Hybrid Conductive Fiber with 500%-Strain Electric Stability and Deformation-Independent Linear Temperature Response

Jianpeng Wu, Min Sang, Jingyi Zhang, Yuxi Sun, Xinyi Wang, Junshuo Zhang, Haoming Pang, Tianzhi Luo, Shaoshan Pan, Shouhu Xuan,* and Xinglong Gong*

Supporting Information

Ultra-stretchable spiral hybrid conductive fiber with 500%-strain electric stability and deformation-independent linear temperature response

Jianpeng Wu, Min Sang, Jingyi zhang, Yuxi Sun, Xinyi Wang, Junshuo Zhang, Tianzhi Luo, Shaoshan Pan, Shouhu Xuan*, and Xinglong Gong*

J. P. Wu, M. Sang, J. Y. Zhang, Y. X. Sun, X. Y. Wang, J. S. Zhang, Prof. T. Z. Luo, S. S. Pan, Prof. S. H. Xuan, Prof. X. L. Gong
CAS Key Laboratory of Mechanical Behavior and Design of Materials, Department of Modern Mechanics, University of Science and Technology of China (USTC), Hefei, Anhui 230027, PR China
E-mail: xuansh@ustc.edu.cn (S. H. Xuan), gongxl@ustc.edu.cn (X. L. Gong)

Prof. S. H. Xuan, Prof. X. L. Gong
State Key Laboratory of Fire Science, University of Science and Technology of China (USTC), 96 Jinzhai Road, Hefei, Anhui 230026, PR China
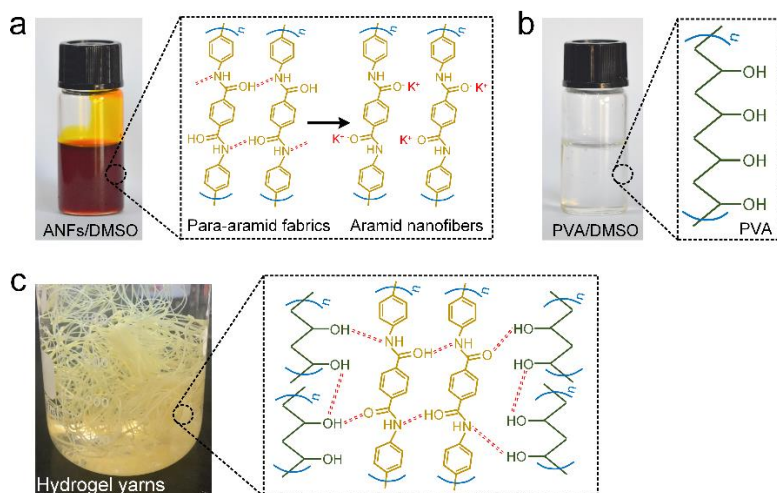
Figure S1. Photographs and illustrations of the preparation mechanism of hydrogel yarns. a) Photograph of ANFs/DMSO and the deprotonation process of ANFs (Red dotted lines represent hydrogen bonds). b) Photograph of PVA/DMSO and corresponding PVA molecular chain. c) Photograph of hydrogel yarns and the hydrogen bond interactions among PVA and ANFs chains.
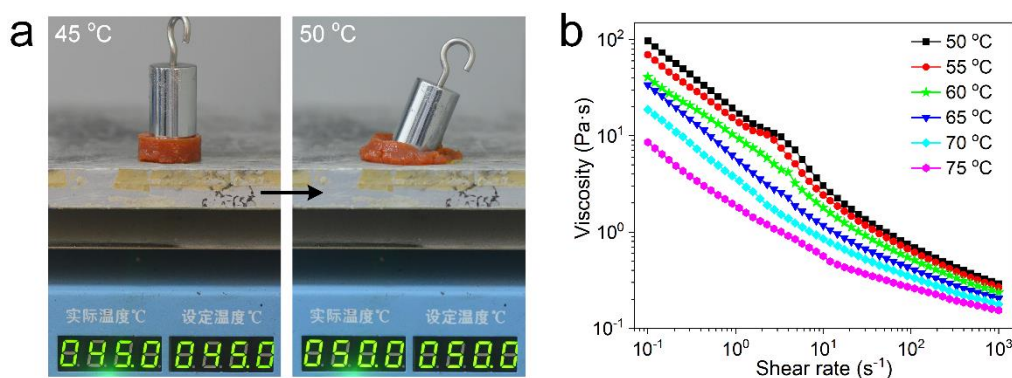

Figure S2. Temperature-dependent rheological property of ANFs/PVA/DMSO mixture. a) Photographs of ANFs/PVA/DMSO mixture. This mixture collapsed at 50 ℃ and could not support the weight (50 g), indicating its phase transition from viscoelastic state to fluid state at ~50 ℃. b) Viscosity of ANFs/PVA/DMSO mixture with different temperatures as a function of shear rate.
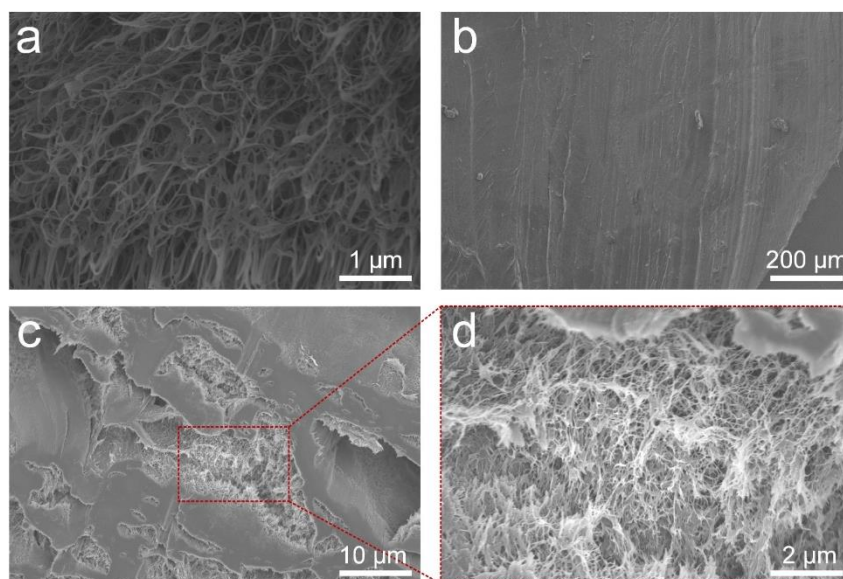
Figure S3. Characterizations of ANFs, PVA, and ANFs/PVA. SEM images of a) ANFs and b) PVA. Cross-sectional SEM image of c) ANFs/PVA hydrogel yarn and d) corresponding magnified view.
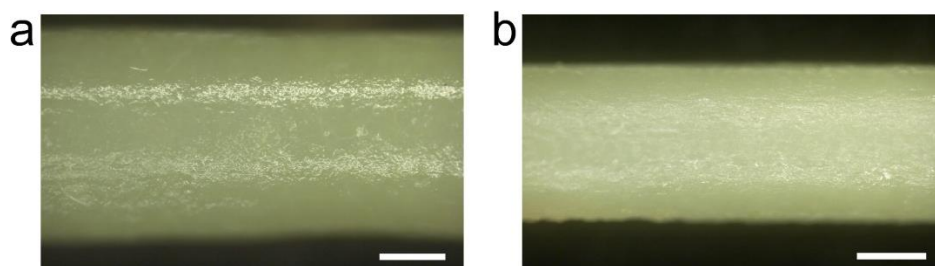

Figure S4. Characterizations of hydrogel yarns. Optical micrographs of longitudinal surfaces of hydrogel yarns b) with and a) without drawing. Scale bars, 500 μm.
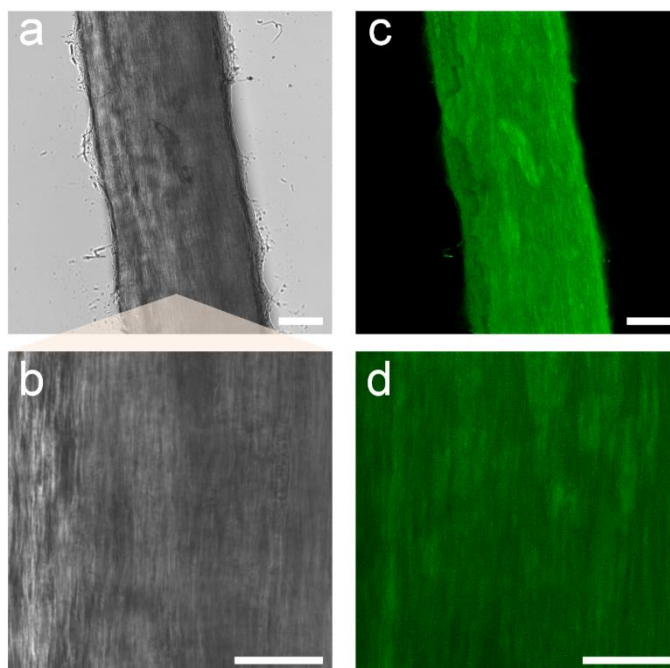
Figure S5. Oriented microstructure of hydrogel yarn. a,b) Optical micrographs of hydrogel yarns after drawing. c,d) Corresponding confocal images. Scale bars, 20 μm.
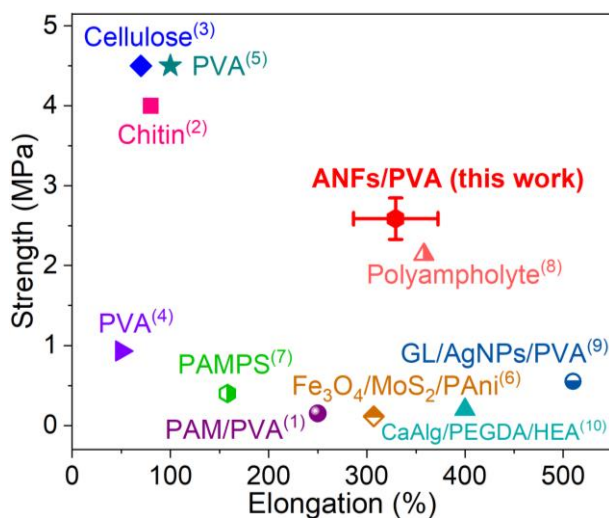

Figure S6. Comparison of ANFs/PVA hydrogel yarns in this work with previous PVA-based hydrogels and other tough hydrogels.[1-10] PAM: polyacrylamide. PANI: polyaniline. PAMPS: poly(2-acrylamido-2-methyl-1-propanesulfonic acid). GL: glycyrrhiza acid. AgNPs: Ag nanoparticles. CaAlg: calcium alginate. PEGDA: (poly(ethylene glycol) diacrylate. HEA: 2-hydroxyethyl acrylate. Error bar represent standard deviation.
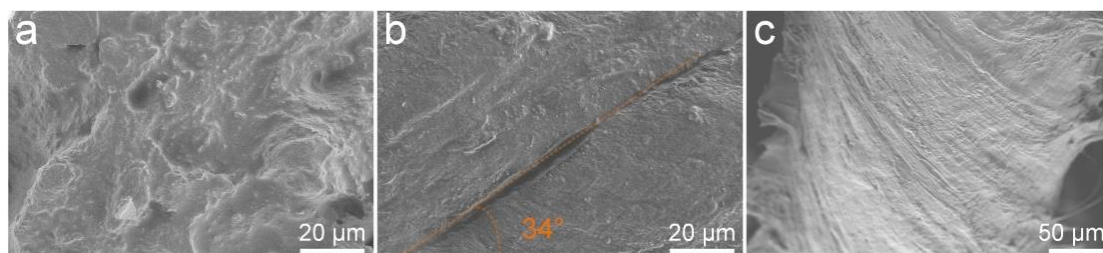
Figure S7. Characterizations of hybrid fibers. SEM images of a) cross section of straight hybrid fiber, b) bias interface of twisted hybrid fiber, and c) distorted microfibrils of spiral hybrid fiber.
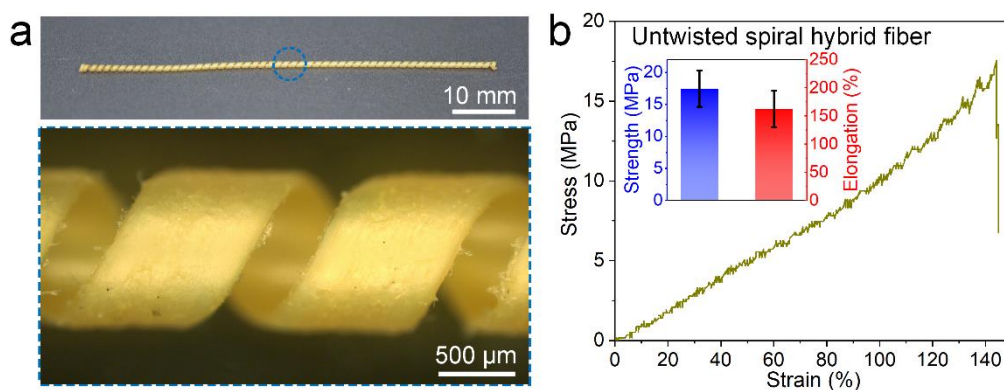

Figure S8. Morphology and mechanical performance of untwisted spiral hybrid fiber. a) Photograph and optical micrograph of untwisted spiral hybrid fiber. b) Tensile property of untwisted spiral hybrid fibers. Error bars represent standard deviation.
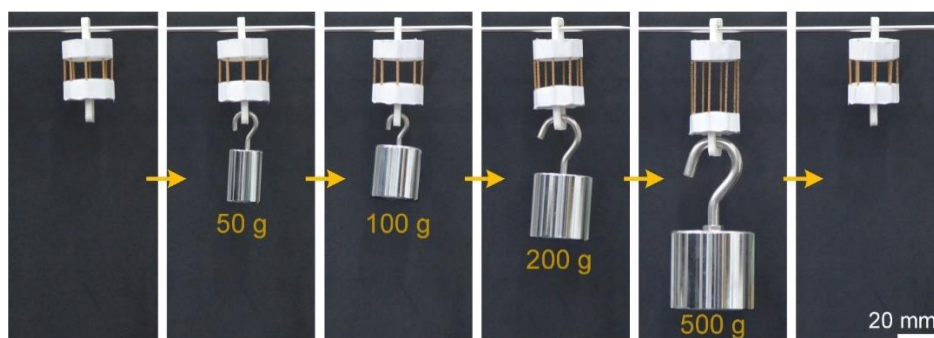

Figure S9. Photographs showing the excellent elasticity and recoverability of spiral hybrid fibers.
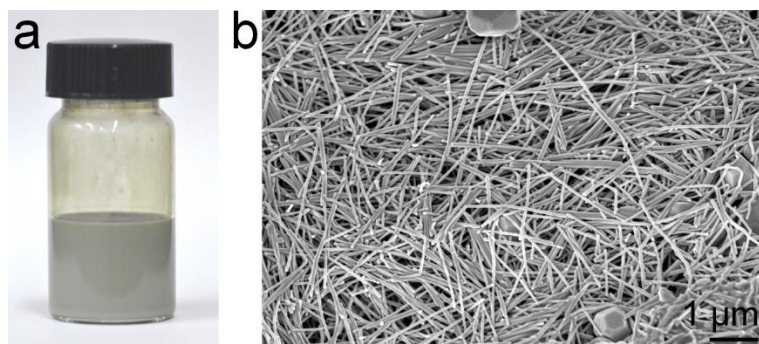
Figure S10. Characterization of self-prepared AgNWs. a) Photograph of grey-green AgNWs/ethanol dispersion. b) SEM images of AgNWs.
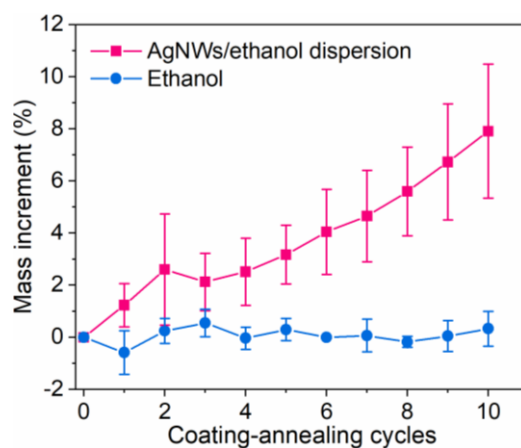
Figure S11. Mass increment of spiral hybrid fiber after 10 coating-annealing cycles. Four samples were tested for each condition. Error bars represent standard deviation.

The spiral hybrid fiber exhibited slight mass increment (7.91%) after coating in AgNWs/ethanol dispersion for 10 cycles. As comparison, when it was dipped in ethanol, the mass hardly changed. So it can be deduced that AgNWs had a negligible impact on the light-weight feature of SHCF through the coating-annealing treatment.

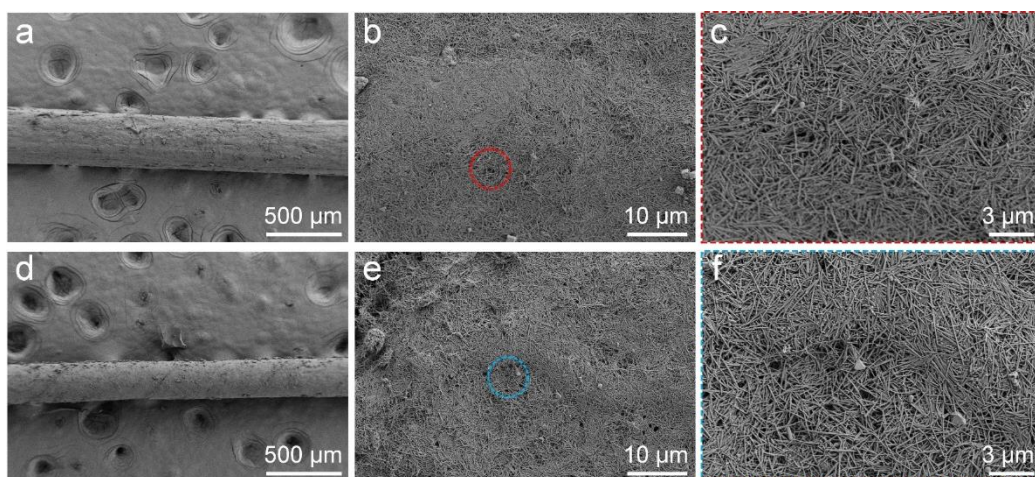**Figure S12.** Characterizations of hybrid conductive fibers. SEM images of a) straight hybrid conductive fiber d) and twisted hybrid conductive fiber. Enlarged views showing the deposited AgNWs on b,c) straight hybrid conductive fiber and e,f) twisted hybrid conductive fiber.
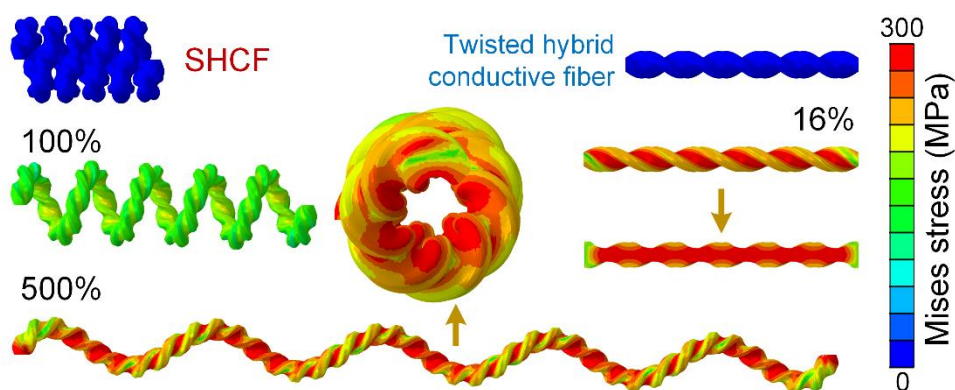

Figure S13. Distributions of mises stress in uniaxial tensile FEM models of SHCF and twisted hybrid conductive fiber.
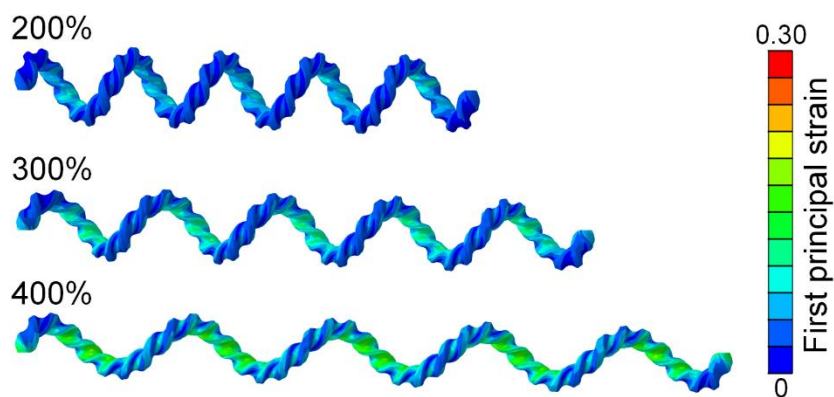
Figure S14. First principal strain distributions of SHCF at 200%-400% strains.
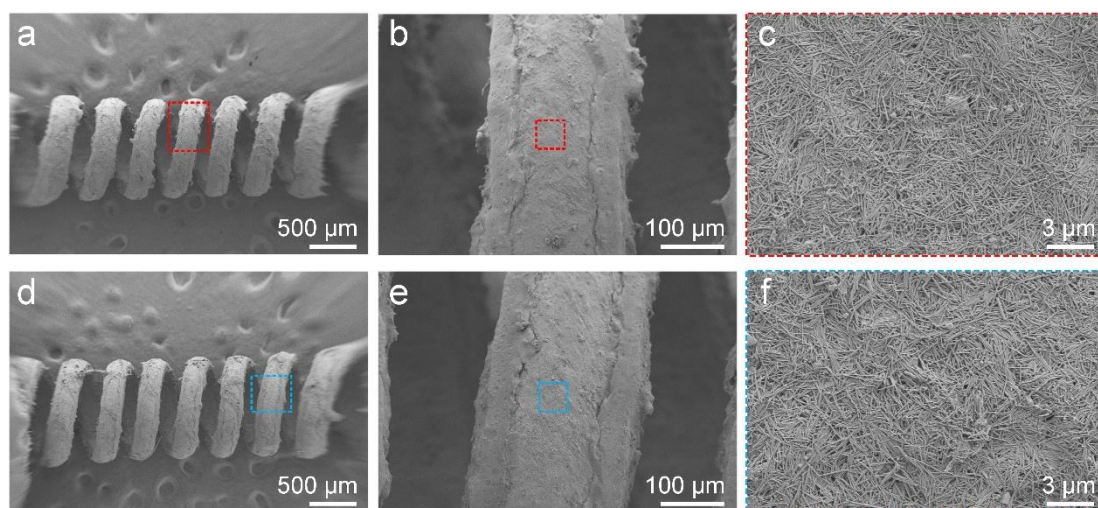
Figure S15. Morphological change of SHCF after cyclic stretching. SEM images of SHCF a,b) before and d,e) after 5000 tensile cycles at 50% strain. The deposited AgNWs on SHCF c) before and f) after tensile cycles.

The micrographs of SHCF before and after 5000 tensile cycles at 50% strain were shown in Figure S15. The homochiral coiled structures in Figure S15a and d were highly consistent owing to the excellent resilience of SHCF. The deposited AgNWs on the fiber surface (Figure S15c and f) also showed good integrity without any slippage or crack after cyclic stretching. These results confirmed the long-term structural stability of SHCF.
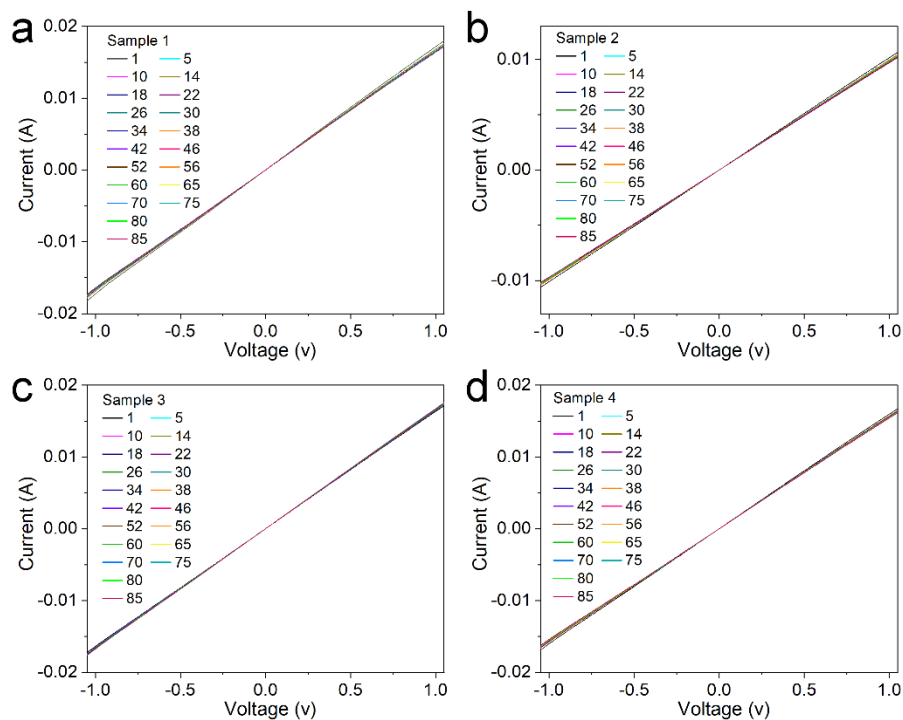
Figure S16. Current-voltage curves of four SHCFs exposed to air. The numbers in charts represent days.
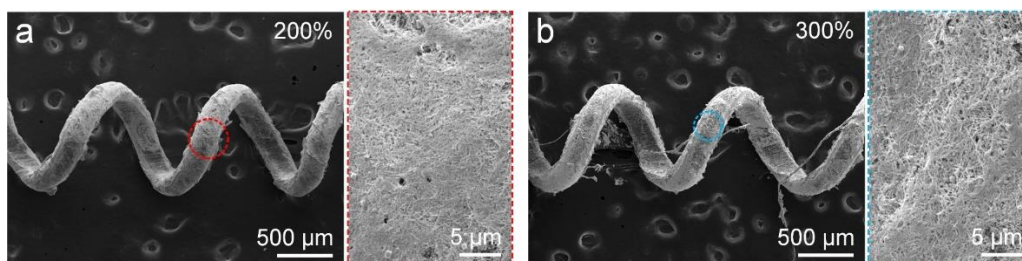
Figure S17. Morphologies of SHCFs at different tensile states. SEM images of SHCFs at a) 200% strain and b) 300% strain. Dashed boxes represent the densely deposited AgNWs.
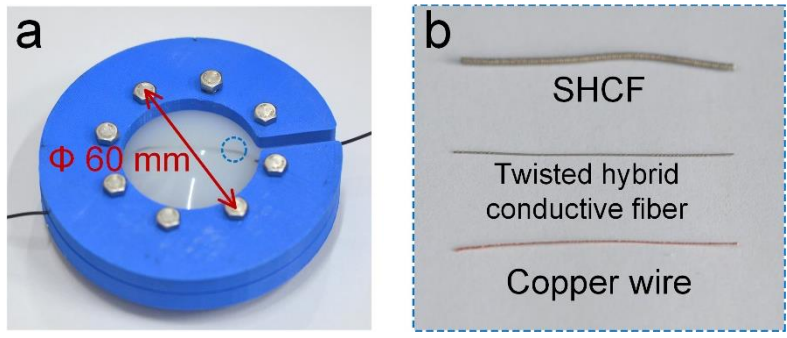
Figure S18. Device for impact test. a) Photograph of Ecoflex embedded with SHCF. b) Photographs of SHCF, twisted hybrid conductive fiber, and copper wire.
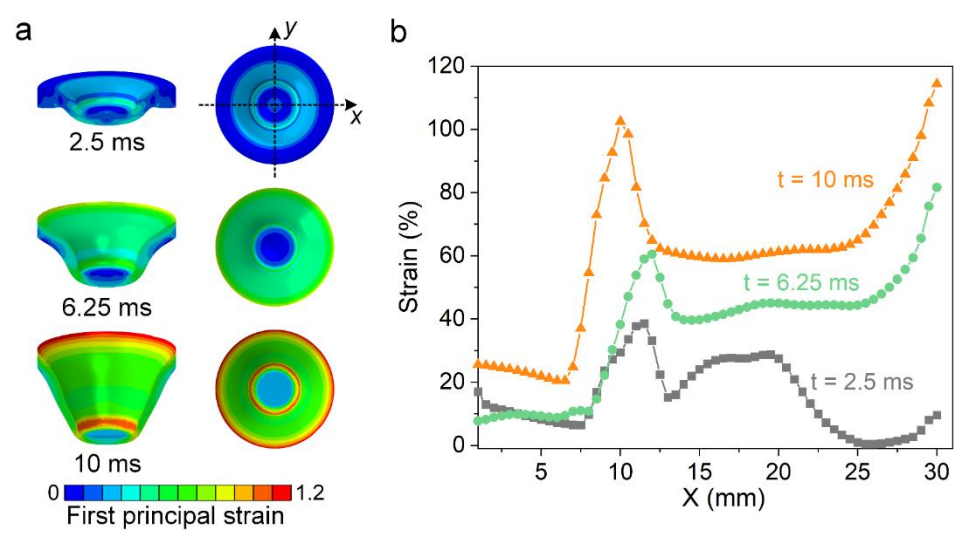
Figure S19. Impact simulation of Ecoflex. a) Strain nephograms of Ecoflex at central cross-section (left side) and impact surface (right side) at different moments after hammer contacted sample. b) Strain distributions in impact surface along x axis ($y = 0$) at different moments.
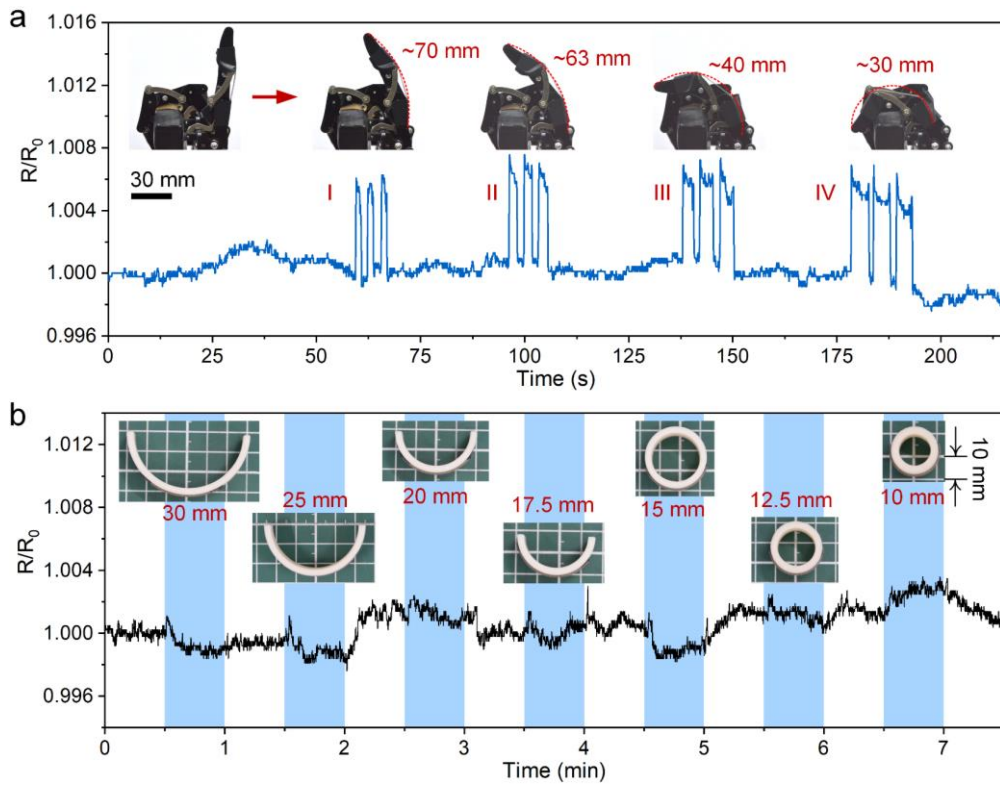
Figure S20. a) Variation in R/R_0 of SHCF attached on a robotic finger under four bending degrees. Insets represent the bending radius at ~70 mm, ~63 mm, ~40 mm, and ~30 mm, respectively. b) Variation in R/R_0 of SHCF attached on circular surfaces (blue regions). Insets represent the bending radius at 30 mm, 25 mm, 20 mm, 17.5 mm, 15 mm, 12.5 mm, and 10 mm, respectively.

Generally, small bending radius of robotic hand would induce large tensile deformation of SHCF. The electrical variation of SHCF at four bending radii (~70 mm, ~63 mm, ~40 mm, and ~30 mm) was measured. As shown in Figure S20a, although the bending radius deceased from ~70 mm to ~30 mm successively, R/R_0 kept similar change trend. The maximum variation was also no more than 1.008, reflecting the robust electrical stability against large bending degree. In addition, the minimum bending radius of ~30 mm was used to demonstrate the cyclic bending of robotic finger (Figure 5i). Furthermore, the pure bending of SHCF was investigated by attaching it on different circular surfaces without tension (Figure S20b). The electrical variation (R/R_0) was no more than 1.004 when the bending radius gradually decreased

from 30 mm to 10 mm. Therefore, SHCF exhibited robust electrical stability in both tensile and bending deformations.

Figure S21. Morphology changes of SHCFs after 150 000 cyclic bending.
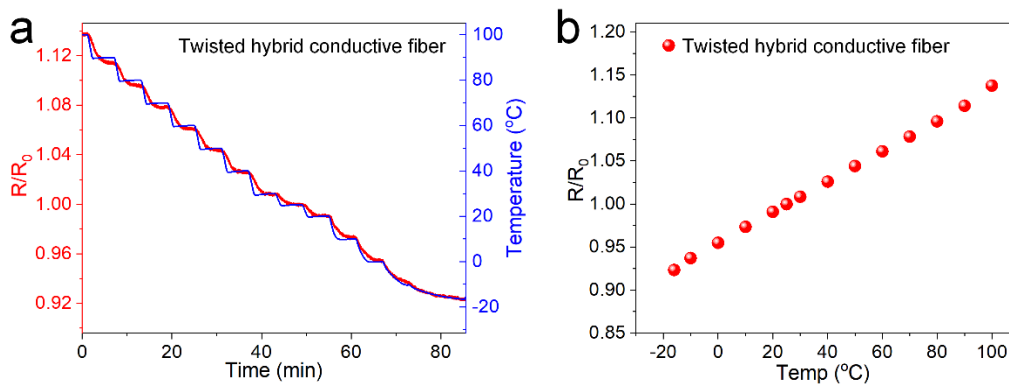

Figure S22. Temperature perception of twisted hybrid conductive fiber. a) R/R_0 of twisted hybrid conductive fiber and test temperature as a function of time. b) Corresponding temperature sensing data.
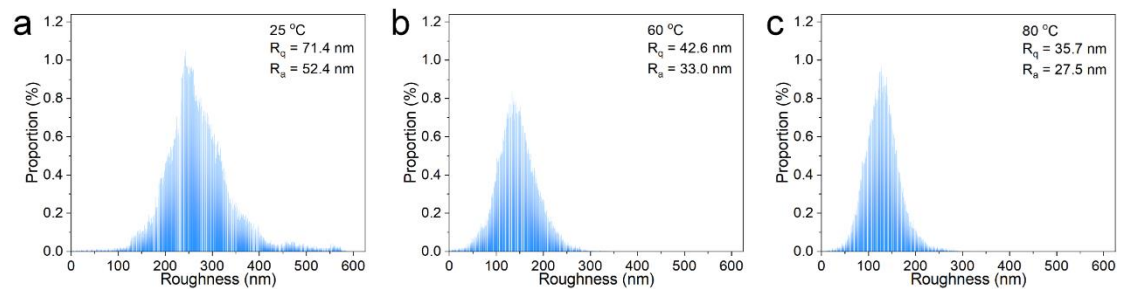
Figure S23. Characterization of stack morphologies of AgNWs on SHCF. Roughness of deposited AgNWs extracted from AFM images in Figure 6a at a) 25 °C, b) 60 °C,

and c) 80 °C. R_q: root mean squared value of deviations of profile; R_a: arithmetic average of deviations from the mean of roughness.
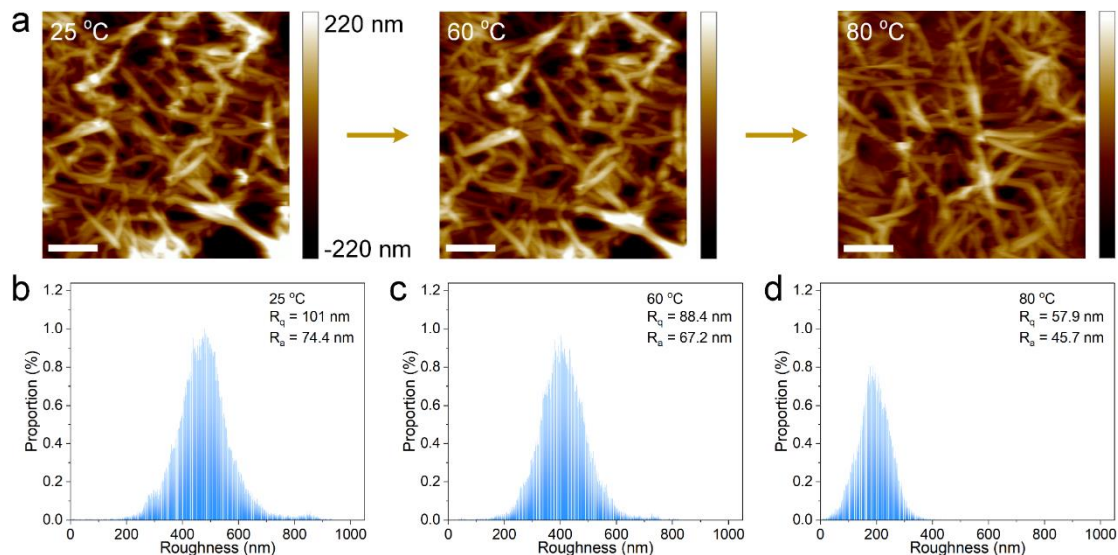
Figure S24. Characterization of stack morphologies of AgNWs on twisted hybrid conductive fiber. a) AFM images of deposited AgNWs on fiber matrix. Corresponding roughness of deposited AgNWs at b) 25 °C, c) 60 °C, and d) 80 °C. All color bars have the same height range (-220 to 220 nm). When the test temperature increased from 25 to 80 °C, AgNWs became gradually clear and the R_q declined from 101 nm to 57.9 nm, implying the thermal-induced stack densification of AgNWs on fiber matrix surface.
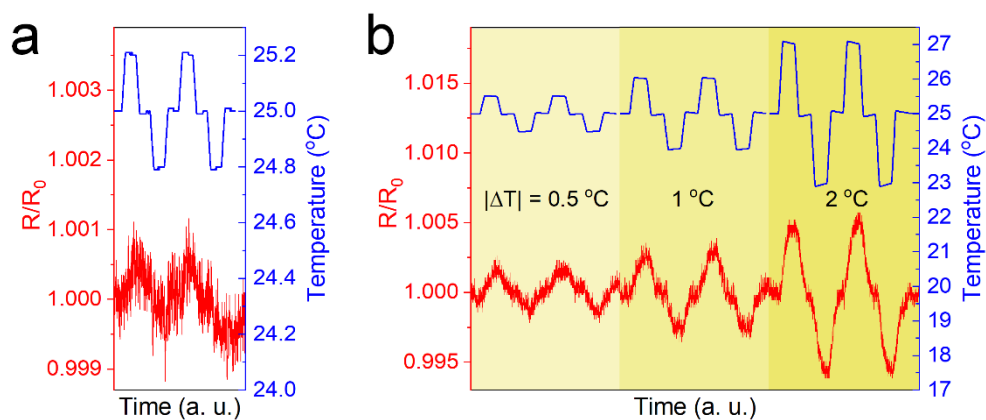
Figure S25. Electrical responses of SHCF to tiny temperature variations based on

25 °C. The temperature changes ($|\Delta T|$) were a) 0.2 °C, b) 0.5 °C, 1 °C, and 2 °C, respectively.
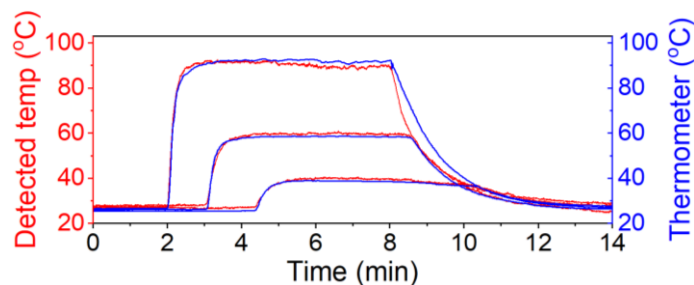
Figure S26. Temperature curves measured by SHCF and commercial metal thermometer, respectively. Red curves represent the temperatures measured by SHCF.
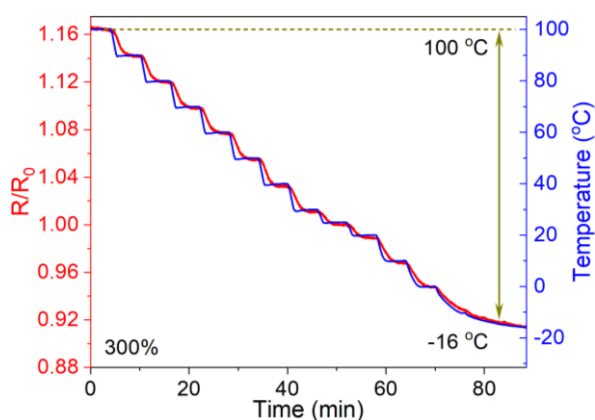
Figure S27. Temperature sensing curve of SHCF at 300% strain.
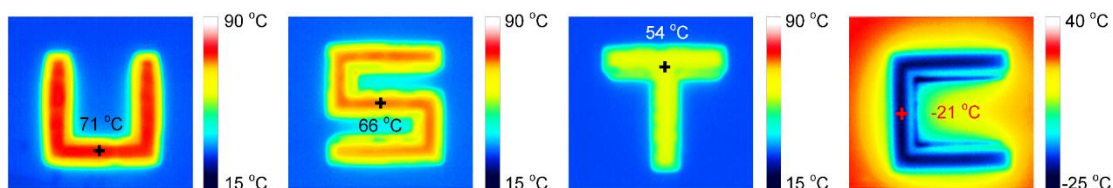
Figure S28. Thermographic images of letter-like water containers. The water temperatures were ~71 °C ("U"), ~66 °C ("S"), ~54 °C ("T"), and ~-21 °C ("C", cooled with liquid nitrogen) respectively.
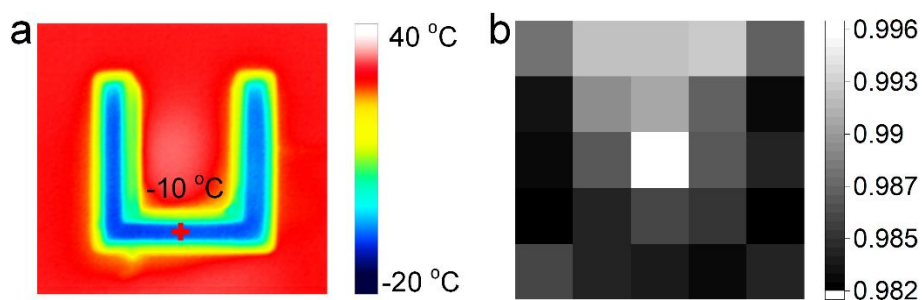
Figure S29. Temperature perception of sensing array to "U"-like water container. a) Thermographic image of "U"-like water container (~-10 °C). b) Corresponding color heat map detected by sensor array. The numbers in color bar represent the value of R/R_0.
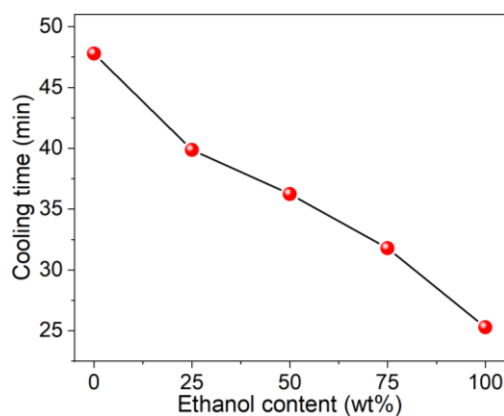
Figure S30. Cooling times of aqueous solutions as a function of ethanol content.
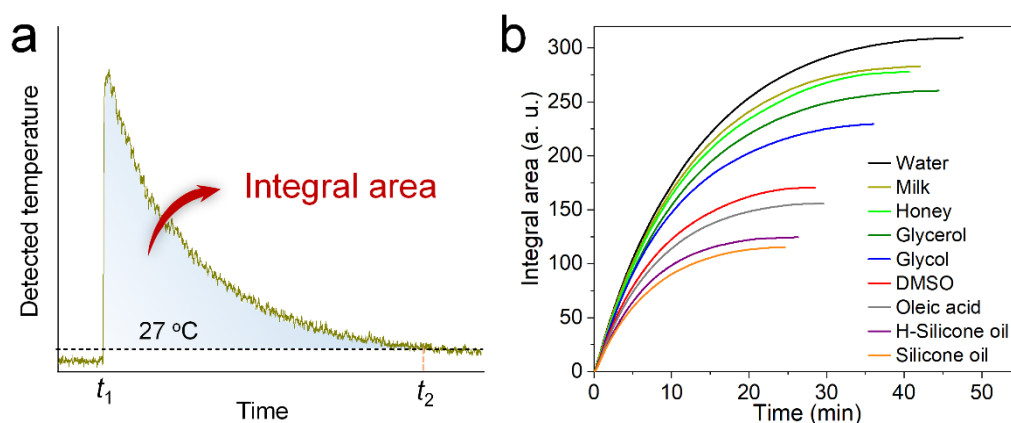
Figure S31. Heat dissipation assessment to various liquids *via* integral area. a) Illustration of the integral area from t_1 (the moment of liquid injection) to t_2 (the moment of liquid reaching 27 °C) of temperature curve. b) Integral areas over time of

tested liquids.
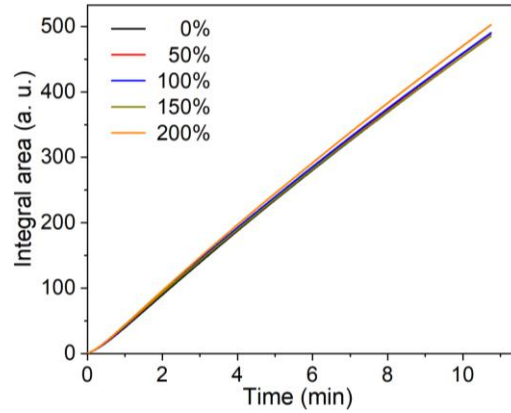
Figure S32. Integral areas over time of temperature curves measured by SHCFs at different tensile strains (0%-200%).

Table S1. Comparison of SHCF with reported stretchable conductors. Data are presented as average value with standard deviation. (N/A: not applicable)

Materials	Maximum change of R/R_0 or C/C_0	Corresponding tensile strain (%)	Maximum strain (%)	Configuration	Ref.
Au-doped silicone nanomembrane	1.007	30	N/A	Serpentine mesh circuit	[11]
Ni-GaIn amalgam	1.9	70	N/A	LM-based coil circuit	[12]
LM nanoparticle-PDMS	2	160	N/A	PDMS-encapsulated LM film	[13]
LM-Ecoflex-Vytaflex	4.5	700	700	LM-embedded elastomer	[14]
Cu-EGaIn e-skin	4.22	100	N/A	Cu-EGaIn circuit-embedded Ecoflex	[15]
LM-TPU	4.5	570	570	Water-net structure	[16]
LM-PDMS	1.04305	116.86	116.86	3D-Calabash Bunch structure	[17]
Ag-EGaIn-PVA	1.5	60	56.7 ± 4.2	EGaIn-coated Ag particles embedded in PVA gel	[18]
AgNWs-PDMS	1.375	180	N/A	Buckled nanowire networks	[19]
LM-polyurethane	3	500	N/A	LM droplets embedded in polyurethane matrix	[20]
LM-PDMS	1.11	50	N/A	3D-interconnected networks of porous sponge	[21]
AgNWs-PDMS	0.97	100	N/A	Buckle-delaminated AgNWs	[22]

| | | | | circuit on PDMS film | |
| Spiral Ag-coated ANFs/PVA fiber | 1.02 ± 0.05 | 500 | 958.2 ± 75 | Homochiral coiled structure | **This work** |

*Au: gold; Ni: nickel; GaIn: gallium indium alloy; LM: liquid metal; PDMS: polydimethylsiloxane; Cu: copper; EGaIn: gallium indium eutectic alloy; TPU: thermoplastic polyether urethanes.

Table S2. Comparison of SHCF with reported temperature sensors.

Materials	Sensing range (℃)	Minimum resolution (℃)	Response characteristic	Sensing mechanism	Ref.
Ni-NiO-Ni circuit	25 to 70	1	Exponential	Nickel vacancy compensation	[23]
PANI-glycerol hydrogel	40 to 110	2.7	Linear, $R^2 = 0.99$	Thermosensation of PANI nanofibers	[24]
PENB-F4TCNQ	20 to 90	2	Linear with two regions	Donor-acceptor	[25]
Multilayer CNF films	25 to 50	1	Linear	Metallic nature-yielded positive temperature coefficient	[26]
Pentacene-AgNPs	20 to 100	0.4	Exponential	Two-terminal thermistor AgNPs	[27]
PAM-carrageenan hydrogel	25 to 70	0.77	Linear	Thermistor double network	[28]
Kirigami AgNWs-TPU	5 to 50	0.14	Linear, $R^2 = 0.998$	Thermal expansion of TPU	[29]
PDMS-encapsulated PAM-carrageenan	-28 to 95.3	0.8	Nonlinear	Geometry and phase-changing effect and ions accumulation	[30]
Graphene hydrogel	26 to 101	0.2	Exponential	Thermistor graphene	[31]
CNT-InGaZnO circuits	20 to 45	0.3	Linear	Temperature dependence of CMOS	[32]
pNIPAM-PEDOT:PSS-CNT	20 to 40	0.5	Linear, $R^2 = 0.98$	Temperature-dependent swelling-deswelling effect	[33]
Spiral Ag-coated ANFs/PVA fiber	-20 to 100	0.2	Linear, $R^2 = 0.9998$	Thermal-induced stack densification of AgNWs	**This work**

*Ni: nickel; NiO: nickel oxide; PANI: polyaniline; PENB: donor-acceptor polymer; F4TCNQ: 2,3,5,6-tetrafluoro-7,7,8,8-tetracyanoquinodimethane; CNF: carbon nanofiber; AgNPs: silver nanoparticles; PAM: polyacrylamide; CNT: carbon nanotube; CMOS: complementary metal-oxide-semiconductor; pNIPAM: poly (N-isopropylacrylamide); PEDOT:PSS: poly (3,4-ethylenedioxythiophene) polystyrene sulfonate.

Supplementary References

[1] R. Bai, J. Yang, X. Morelle, Z. Suo, *Macromol. Rapid Comm.* **2019**, *40*, 1800883.

[2] D. Xu, J. Huang, D. Zhao, B. Ding, L. Zhang, J. Cai, *Adv. Mater.* **2016**, *28*, 5844.

[3] D. Zhao, J. Huang, Y. Zhong, K. Li, L. Zhang, J. Cai, *Adv. Funct. Mater.* **2016**, *26*, 6279.

[4] K. Voges, C. Hubner, M. Vadala, D. Lupascu, *Macromol. Mater. Eng.* **2018**, *303*, 1800198.

[5] S. Lin, X. Liu, J. Liu, H. Yuk, H. Loh, G. Parada, C. Settens, J. Song, A. Masic, G. McKinley, X. Zhao, *Sci. Adv.* **2019**, *5*, eaau8528.

[6] H. Hu, X. Zhong, S. Yang, H. Fu, *Compos. Part B-Eng.* **2020**, *182*, 107623.

[7] Y. Ding, J. Zhang, L. Chang, X. Zhang, H. Liu, L. Jiang, *Adv. Mater.* **2017**, *29*, 1704253.

[8] T. Long, Y. Li, X. Fang, J. Sun, *Adv. Funct. Mater.* **2018**, *28*, 1804416.

[9] H. Zhang, N. Tang, X. Yu, Z. Guo, Z. Liu, X. Sun, M. Li, J. Hu, *Chem. Eng. J.* **2022**, *430*, 132779.

[10] J. Song, S. Chen, L. Sun, Y. Guo, L. Zhang, S. Wang, H. Xuan, Q. Guan, Z. You, *Adv. Mater.* **2020**, *32*, 1906994.

[11] M. Sang, K. Kang, Y. Zhang, H. Zhang, K. Kim, M. Cho, J. Shin, J. Hong, T. Kim, S. Lee, W. Yeo, J. Lee, T. Lee, B. Xu, K. Yu, *Adv. Mater.* **2022**, *34*, 2105865.

[12] R. Guo, X. Wang, H. Chang, W. Yu, S. Liang, W. Rao, J. Liu, *Adv. Eng. Mater.* **2018**, *20*, 1800054.

[13] Y. Yang, J. Han, J. Huang, J. Sun, Z. Wang, S. Seo, Q. Sun, *Adv. Funct. Mater.* **2020**, *30*, 1909652.

[14] M. Bartlett, A. Fassler, N. Kazem, E. Markvicka, P. Mandal, C. Majidi, *Adv. Mater.* **2016**, *28*, 3726.

[15] R. Guo, B. Cui, X. Zhao, M. Duan, X. Sun, R. Zhao, L. Sheng, J. Liu, J. Lu, *Mater. Horiz.* **2020**, *7*, 1845.

[16] J. Cao, F. Liang, H. Li, X. Li, Y. Fan, C. Hu, J. Yu, J. Xu, Y. M. Yin, F. Li, D. Xu, H. Feng, H. Yang, Y. Liu, X. Chen, G. Zhu, R. Li, *Infomat* **2022**, *4*, e12302.

[17] Z. Yu, J. Shang, X. Niu, Y. Liu, G. Liu, P. Dhanapal, Y. Zheng, H. Yang, Y. Wu, Y. Zhou, Y. Wang, D. Tang, R. Li, *Adv. Electron. Mater.* **2018**, *4*, 1800137.

[18] P. Lopes, H. Paisana, A. De Almeida, C. Majidi, M. Tavakoli, *ACS Appl. Mater. Inter.* **2018**, *10*, 38760.

[19] B. Kim, H. Kwon, H. Kwon, J. Pyo, J. Oh, S. Hong, J. Park, K. Char, J. Ha, J. Son, S. Lee, *Adv. Funct. Mater.* **2020**, *30*,1910214.

[20] R. Zheng, Y. Wu, Y. Xu, S. Liu, H. Liu, P. Wang, Z. Deng, S. Chen, L. Liu, *Mater. Lett.* **2019**, *235*, 133.

[21] S. Liang, Y. Li, Y. Chen, J. Yang, T. Zhu, D. Zhu, C. He, Y. Liu, S. Handschuh-Wang, X. Zhou, *J. Mater. Chem. C* **2017**, *5*, 1586.

[22] S. Wu, S. Yao, Y. Liu, X. Hu, H. Huang, Y. Zhu, *ACS Appl. Mater. Inter.* **2020**, *12*, 41696.

[23] J. Shin, B. Jeong, J. Kim, V. Nam, Y. Yoon, J. Jung, S. Hong, H. Lee, H. Eom, J. Yeo, J. Choi, D. Lee, S. Ko, *Adv. Mater.* **2020**, *32*, 1905527.

[24] G. Ge, Y. Lu, X. Qu, W. Zhao, Y. Ren, W. Wang, Q. Wang, W. Huang, X. Dong, *ACS Nano* **2020**, *14*, 218.

[25]   J. Ngai, J. Polena, D. Afzal, X. Gao, M. Kapadia, Y. Li, *Adv. Funct. Mater.* **2022**, *32*, 2110995.

[26]   J. Lee, E. Kim, H. Zhang, H. Chen, H. Venkatesan, K. Chan, J. Yang, X. Shen, J. Yang, S. Jeon, J. Kim, *Adv. Funct. Mater.* **2022**, *32*, 2107570.

[27]   X. Ren, K. Pei, B. Peng, Z. Zhang, Z. Wang, X. Wang, P. Chan, *Adv. Mater.* **2016**, *28*, 4832.

[28]   J. Wu, S. Han, T. Yang, Z. Li, Z. Wu, X. Gui, K. Tao, J. Miao, L. Norford, C. Liu, F. Huo, *ACS Appl. Mater. Inter.* **2018**, *10*, 19097.

[29]   Y. Yu, S. Peng, Z. Sha, T. Cheng, S. Wu, C. Wang, *J. Mater. Chem. A* **2021**, *9*, 24874.

[30]   Z. Wu, H. Ding, K. Tao, Y. Wei, X. Gui, W. Shi, X. Xie, J. Wu, *ACS Appl. Mater. Inter.* **2021**, *13*, 21854.

[31]   J. Wu, W. Huang, Y. Liang, Z. Wu, B. Zhong, Z. Zhou, J. Ye, K. Tao, Y. Zhou, X. Xie, *Adv. Electron. Mater.* **2021**, *7*, 2001084.

[32]   W. Honda, S. Harada, S. Ishida, T. Arie, S. Akita, K. Takei, *Adv. Mater.* **2015**, *27*, 4674.

[33]   J. Oh, S. Hong, H. Park, S. Jin, Y. Jeong, S. Oh, J. Yun, H. Lee, J. Kim, J. Ha, *ACS Appl, Mater. Inter.* **2018**, *10*, 7263.